White Rose Research Online

eprints@whiterose.ac.uk
https://eprints.whiterose.ac.uk
Universities of Leeds, Sheffield and York

Deposited via The University of Sheffield.

White Rose Research Online URL for this paper:
https://eprints.whiterose.ac.uk/id/eprint/238816/

Version: Published Version

Article:
Keys, P.H., Campbell, R.J., Magill, D.K.J. et al. (2026) Small-scale bright point characteristics at high-resolution with the Daniel K. Inouye solar telescope. The Astrophysical Journal, 999 (2). 201. ISSN: 0004-637X

https://doi.org/10.3847/1538-4357/ae2be4

Reuse
This article is distributed under the terms of the Creative Commons Attribution (CC BY) licence. This licence allows you to distribute, remix, tweak, and build upon the work, even commercially, as long as you credit the authors for the original work. More information and the full terms of the licence here: https://creativecommons.org/licenses/

Takedown
If you consider content in White Rose Research Online to be in breach of UK law, please notify us by emailing eprints@whiterose.ac.uk including the URL of the record and the reason for the withdrawal request.

UNIVERSITY OF LEEDS
University of Sheffield
UNIVERSITY of York

The Astrophysical Journal, 999:201 (14pp), 2026 March 10 https://doi.org/10.3847/1538-4357/ae2be4
© 2026. The Author(s). Published by the American Astronomical Society.
OPEN ACCESS

Small-scale Bright Point Characteristics at High-resolution with the Daniel K. Inouye Solar Telescope

Peter H. Keys[1], Ryan J. Campbell[1], Dylan K. J. Magill[1], Mateus A. Keating[1], Mihalis Mathioudakis[1], David B. Jess[1], Damian J. Christian[2], Arthur Berberyan[3], Samuel D. T. Grant[1], Shahin Jafarzadeh[1], Marco Stangalini[4], and Robertus Erdélyi[5,6,7]

[1] Astrophysics Research Centre, Queen's University of Belfast, Belfast, Northern Ireland, BT7 1NN, UK
[2] Department of Physics and Astronomy, California State University Northridge, Nordhoff Street, Northridge, CA 91330, USA
[3] Department of Astronomy & Astrophysics, University of California San Diego, La Jolla, CA 92093, USA
[4] Italian Space Agency (ASI), Via del Politecnico snc, 00133 Roma, Italy
[5] Solar Physics & Space Plasma Research Centre (SP2RC), School of Mathematical and Physical Sciences, University of Sheffield, Hounsfield Road, Sheffield, S3 7RH, UK
[6] Department of Astronomy, Eötvös Loránd University, Pázmány Péter sétány 1/A, H-1117 Budapest, Hungary
[7] Gyula Bay Zoltán Solar Observatory (GSO), Hungarian Solar Physics Foundation (HSPF), Petőfi tér 3, H-5700 Gyula, Hungary
Received 2025 August 29; revised 2025 December 8; accepted 2025 December 9; published 2026 March 3

Abstract

Bright points (BPs) are small-scale, dynamic features that are ubiquitous across the solar disc and are often associated with the underlying magnetic field. Using broadband photospheric images obtained with the Visible Broadband Imager at the National Science Foundation's Daniel K. Inouye Solar Telescope (DKIST), the properties of BPs have been analyzed with DKIST for the first time at the highest spatial resolutions achievable. BPs were observed to have an average lifetime of 95 ± 29 s and a mean transverse velocity of 1.60 ± 0.41 km s^{-1}. The BPs had a log-normal area distribution with a peak at 2300 km^2. Transverse velocities and lifetimes across the DKIST images were comparable and consistent with previous studies. The area distribution of the DKIST data peaked in areas significantly lower than those from the literature. This was explored further and was observed to be due to an overestimation of BP areas due to the merging of close features when the spatial resolution is reduced, in tandem with possible oversplitting of features in the DKIST images. Furthermore, the effect of variable seeing in the data was determined. This showed that the average spatial resolution of the data was around $0\farcs034 \pm 0\farcs007$, in comparison to the theoretical diffraction limit of $0\farcs022$. Accounting for the influence of seeing, the peak of the area distribution of BPs in the DKIST data was estimated as 4800 km^2, which is still significantly lower than previously observed.

Unified Astronomy Thesaurus concepts: Solar magnetic bright points (1984); Solar magnetic fields (1503); Solar granulation (1498); Solar photosphere (1518)

1. Introduction

Bright points (BPs) are observed throughout the solar cycle and across the entire solar disk. They are often associated with the underlying magnetic field within the intergranular lanes, and are sometimes referred to as magnetic BPs (S. K. Solanki 1993; A. G. de Wijn et al. 2009). The theory of how these features form has been around for some time (E. N. Parker 1978; B. Roberts & A. R. Webb 1978; H. C. Spruit 1979; H. C. Spruit & E. G. Zweibel 1979). The theory posits that magnetic flux is advected into the intergranular lanes, where it concentrates. Fast downflows within the intergranular lanes and pressure differences between the flux tube and the surroundings cause the magnetic flux concentrations to contract until the outward pressure due to the intensified magnetic field balances the external pressures exerted on the flux tube. The equipartition field strength at this point is expected to be on the order of a kilogauss. This process has been referred to as "convective collapse" due to the role of convective processes in enhancing the magnetic field strength. The concentration of the field makes the feature appear pointlike. Then, a combination of heating at the base of the tube from the surrounding hot granular walls and the fact that the tube is partially evacuated means that the intensity of the features will be greater than that of their surroundings.

The convective-collapse process was eventually observationally identified with Hinode data by S. Nagata et al. (2008). The authors found that there was an increased downflow (up to 6 km s^{-1}) in the region of a magnetic field concentration, which then increased the magnetic field strength to 2 kG and enhanced the intensities observed in the *G* band as a BP formed. It should be noted that the *G* band is often used to study BPs, as it has been shown that the abundance of CH molecules is reduced at the higher temperatures experienced within the flux tube of the BP (O. Steiner et al. 2001). Therefore, BPs will tend to appear brighter in *G*-band intensity images in comparison to other photospheric bandpasses.

Theory has suggested that magnetic fields within BPs are of the order of a kilogauss, which has been reported in both simulations and observations (D. B. Jess et al. 2010a; D. Utz et al. 2013; S. Criscuoli & H. Uitenbroek 2014; D. Buehler et al. 2019; M. Cubas Armas & D. Fabbian 2021; to name a few). However, studies have shown that the magnetic field strength of BPs follows a bimodal distribution (D. Utz et al. 2013; P. H. Keys et al. 2019), with a "weak" group at around 300–600 G and a "strong" group at around 1100–1300 G. D. Utz et al. (2014) showed that only 30% of BPs reach kilogauss field strengths. It had been posited (P. H. Keys et al. 2019) that this "weak" group was due to concentrations of magnetic field within the lanes that had yet to undergo

Original content from this work may be used under the terms of the Creative Commons Attribution 4.0 licence. Any further distribution of this work must maintain attribution to the author(s) and the title of the work, journal citation and DOI.

convective collapse, with emerging flux being dispersed before it could amplify to kilogauss strengths. Subsequent work by P. H. Keys et al. (2020) showed that several processes, aside from solely convective collapse, can amplify the field strength and give rise to kilogauss field strengths.

BPs have been estimated as covering ∼0.9%–2.2% of the solar surface (J. Sánchez Almeida et al. 2010), with diameters typically between ∼100–300 km (J. Sánchez Almeida et al. 2004; D. Utz et al. 2009; P. J. Crockett et al. 2010). Furthermore, BPs have been observed to expand with height (M. J. Martínez González et al. 2012; C. Kuckein 2019). Reported lifetimes can vary between 90 s to several minutes depending on the region in which they are found and the characteristics of the observational data (D. Utz et al. 2010; P. H. Keys et al. 2011). BPs are dynamic features with typical transverse velocities of around 1 $\mathrm{km\,s^{-1}}$ (D. Utz et al. 2009; P. H. Keys et al. 2011). BPs can experience rapid excursions above 3 $\mathrm{km\,s^{-1}}$ due to superdiffusive Lévy flights (S. Jafarzadeh et al. 2013), with diffusion in the photosphere linked to the position of the BPs within the network cell. Recently, M. Stangalini et al. (2025) found that the dynamic behaviors of small-scale magnetic field concentrations are modulated by the solar cycle, with temporal scales on the order of 11 yr, although at much lower spatial resolutions (1″) than is commonly achievable with ground-based facilities.

BPs are often seen as important in studying the evolution of magnetic fields at small spatial scales (L. Bellot Rubio & D. Orozco Suárez 2019), as they are interpreted as tracers of flux-tube footpoints (Y. Yang et al. 2015). Furthermore, their dynamic behavior and magnetic nature means that they are frequently analyzed in wave studies as a possible source of propagating wave phenomena (D. B. Jess et al. 2023; A. Berberyan et al. 2024). By analyzing high-resolution simulations, P. H. Keys et al. (2021) were able to show that inversions of a BP with a known driver could return accurate atmospheric parameters at the resolution of the Daniel K. Inouye Solar Telescope (DKIST; T. R. Rimmele et al. 2020) in the presence of an upwardly propagating wave. Therefore, the analysis of BPs with DKIST could be beneficial in understanding their contributions to channeling energy to higher regions in the solar atmosphere. Here, we present the first analysis of the characteristics of BPs with DKIST. The study looks at the properties of these BPs at the highest resolution ever obtained.

2. Observations

On 2022 May 26, between 17:46 UT and 19:31 UT, a sequence of quiet-Sun observations at disk center was obtained with the Visible Broadband Imager (VBI; F. Wöger et al. 2021), installed as a common-user instrument at DKIST (T. R. Rimmele et al. 2020) during its first cycle of operations. The observing sequence was chosen to maximize the spatial and temporal capabilities of the instrument to analyze small-scale, short-lived features at the highest possible resolutions. The 2.′8 field stop was employed with a spatial sampling of 0.″011 $\mathrm{pixel^{-1}}$, giving an effective field of view of around 45″ × 45″. Observations were taken with the 4305 Å *G*-band filter at a cadence of around 6.1 s. A sample image of the field of view with a cutout showing a sample of BPs in the image is given in Figure 1.

This observing sequence has associated cospatial images taken with the Ca II K filter with VBI and scans with the Visible Spectropolarimeter (ViSP; A. G. de Wijn et al. 2022) in the Fe I line pair at 6301.5 Å and 6302.5 Å, alongside the Ca II 8542 Å line. Within this study, we limit our analysis to the *G* band, however other aspects of this observing sequence have been studied and detailed elsewhere (e.g., R. J. Campbell et al. 2023). Although the magnetic field can be returned with ViSP, the scan time for these observations, coupled with the expected lifetimes of any identified BPs, means that it would be difficult to return magnetic field distributions for a significant sample of BPs in the data. Furthermore, the dynamic nature of BPs means that there is the potential for BPs to move outside the slit during the scan with ViSP. Studies of BPs with ViSP would then be limited to longer-lived features that are likely to be more static. Also, the spatial resolution of ViSP is approximately an order of magnitude worse than VBI, so spatially resolving BPs would be more challenging. Here, we limit the study to the *G* band due to the superior spatial and temporal resolution with VBI. Additionally, with the *G* band we can more readily compare to previous work, and BPs in the *G* band are generally considered as tracers of the magnetic field, as mentioned previously.

It should be noted that although the sequence ran for around 1 hr and 45 minutes (1034 frames in total), the location of the adaptive optics (AO) lock point shifted at around 90 minutes into the sequence due to a temporary drop in seeing conditions. Therefore, care must be taken when analyzing the continuation of features around this point in the sequence. Seeing conditions were relatively good and consistent across the dataset aside from this temporary drop near the end of the sequence. The data have a mean Fried parameter (r_0) of 12.1 ± 3.1 cm and a range of 10.2–20.9 cm, as reported in the FITS metadata of the images.

The data underwent level 1 processing onsite, whereby the images had been flat and dark-corrected, as well as undergoing speckle reconstruction (F. Wöger et al. 2008) prior to being made publicly accessible. A postspeckle reconstruction pipeline was generated to produce science-ready images from the level 1 data. This pipeline was based on the Rapid Oscillations in the Solar Atmosphere (ROSA; D. B. Jess et al. 2010b) instrument pipeline, which is a similar instrument to VBI, providing multichannel broadband imaging. The pipeline performs image destretching to account for residual atmospheric seeing effects, as well as aligning the data to remove pointing fluctuations and coaligning data between multiple filters for the image sequence. An example of the fully processed data is shown in Figure 1.

3. Methods

BPs were tracked in the *G*-band images using an automated detection and tracking algorithm (P. J. Crockett et al. 2010), which has been employed across several studies to identify features between frames in the *G* band (P. H. Keys et al. 2011, 2014) and other wideband filters (P. H. Keys et al. 2019, 2020). As a short summary, the code works by isolating bright features in an image before using intensity thresholding to determine the boundary locations of BPs and discarding erroneous detections, such as exploding granules or brightenings at the edge of granules due to density enhancements. Due to the scale of the images acquired from DKIST, and the way that memory allocations are handled by the algorithm, the code had to be augmented to improve memory management through parallel processing. Even with these improvements, and the use of high-performance computing to process the

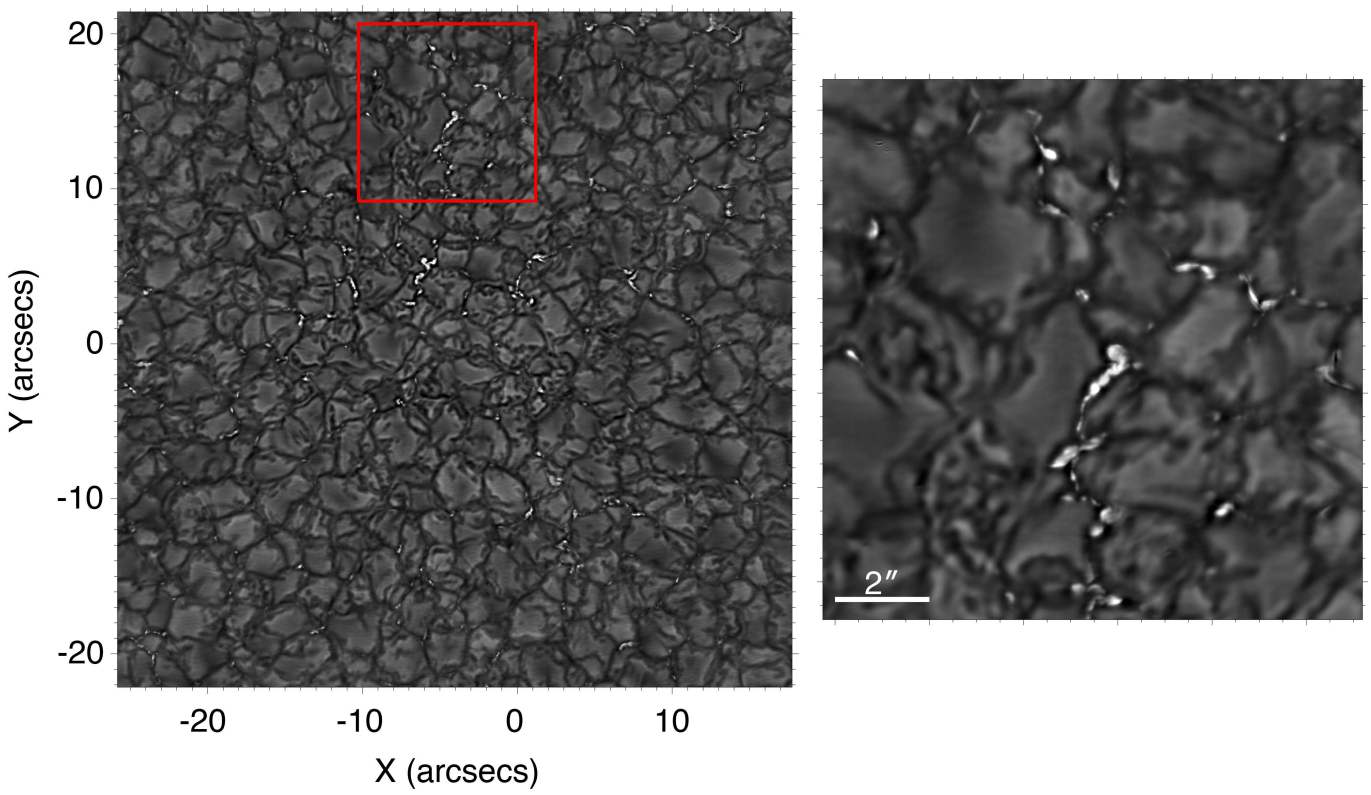

Figure 1. A sample image of the quiet-Sun data obtained with VBI on 2022 May 26 with the *G*-band filter at 17:50 UT. The images have a spatial sampling of 0.″011 pixel^{-1} and a cadence of around 6 s. The estimated spatial resolution of this image is 0.″032 (∼23 km). The full field of view of the image can be seen in the left-hand panel. The red box indicates the region shown in the zoomed-in right-hand panel. The zoom indicates the typical structure and configurations of the BPs under investigation at the resolution of DKIST. Examples of both elongated chains and BP groups, as well as isolated pointlike features, can be seen.

data, this phase took a significant number of compute hours in comparison to similar data from smaller-aperture telescopes (nearly 10 times longer than images from 1 m class telescopes). This is not unexpected, but something to consider for future work.

To compare the DKIST VBI image sequence to similar data from other high-resolution ground-based facilities, the DKIST data were degraded to match the spatial sampling of typical data from GREGOR (L. Kleint et al. 2020), the Swedish Solar Telescope (SST; G. B. Scharmer et al. 2003), and the Dunn Solar Telescope (DST). The approximate spatial sampling for the degraded datasets was 0.″038 pixel^{-1}, 0.″059 pixel^{-1}, and 0.″069 pixel^{-1} for the GREGOR, SST, and DST data, respectively. The spatial degradation was performed using an approach similar to that outlined by R. J. Campbell et al. (2021), with the DKIST observations convolved with theoretical point-spread functions of the respective facilities. The temporal resolution of the degraded data was kept the same as that of the original DKIST data, as each of these facilities can easily acquire data with a 6 s cadence. The degraded datasets were analyzed with the same detection and tracking algorithm as the DKIST data. A sample of the degraded images detailing a zoomed-in example of a BP at these resolutions is included in Figure 2. For simplicity, the degraded data will henceforth be referred to by the facility the data were degraded to match (i.e., GREGOR, SST, and DST), while the original data will be referred to as the DKIST data.

Furthermore, to judge the effect of seeing on the BP established properties, the spatial resolution for each frame of the DKIST data was estimated using the Fourier technique outlined in Appendix A of C. Beck et al. (2007). Figure 3 shows the variation of spatial resolution over time for this particular dataset. The mean spatial resolution across the dataset was found to be 0.″034 ± 0.″007, with the spatial resolution varying from around 0.″023 (close to the theoretical diffraction limit) to 0.″066. It should be noted here that the average spatial resolution at this wavelength would correspond to the diffraction limit of a 3 m class telescope. An estimate of r_0 is given in the image metadata. However, since the value of r_0 depends on where in the Earth's atmosphere the value is estimated, the spatial resolution calculated for each frame via the Fourier approach will give a better indication of image quality. It should of course be noted here that this technique is also not without limitations. The technique involves an estimate of the frequency cutoff to determine the spatial resolution. This choice can be somewhat subjective, and it is possible that some signal may be retained above the identified cutoff, which would result in a lower estimate of the spatial resolution than reported. However, the technique is still likely to be a more reliable estimate of image quality over r_0. For part of the analysis, the spatial resolution in each frame was used to determine the smallest resolvable pixel dimensions for BPs in each frame to filter the subsequent area and velocity estimates of the BPs. Both distributions are discussed below.

With the transverse velocities, the diffusive properties of the BPs were estimated. Several authors have previously looked at the diffusive properties of BPs (A. C. Cadavid et al. 1999; V. I. Abramenko et al. 2011; S. Jafarzadeh et al. 2014). Here, the diffusion index, γ, was estimated by analyzing the squared displacement for each BP over time. With this, the diffusion

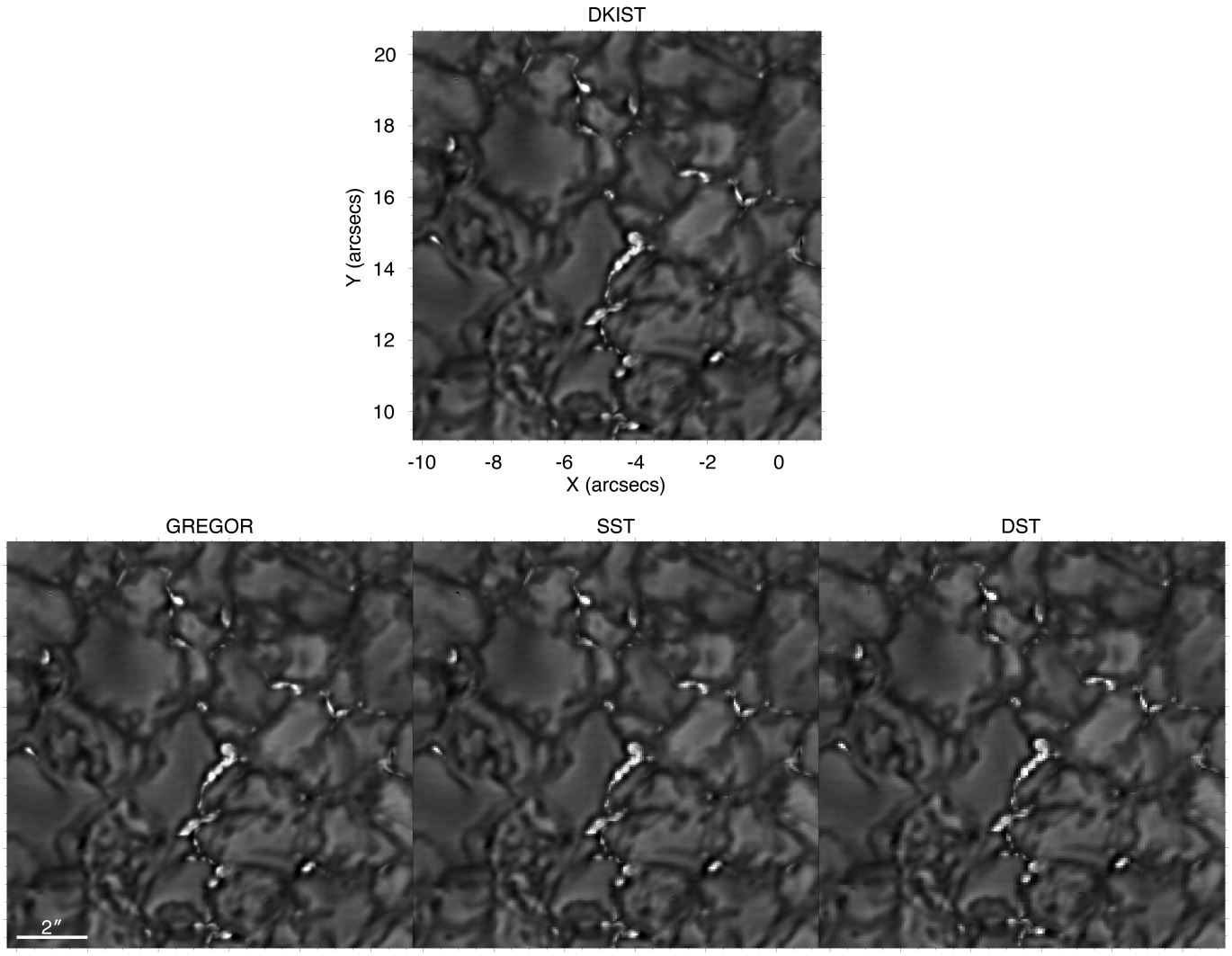

Figure 2. Samples images of the DKIST data degraded to match the resolution of other commonly used ground-based facilities (GREGOR, SST, and DST). Degradation was performed using a similar methodology as outlined in R. J. Campbell et al. (2021). The top panel shows the zoomed image from Figure 1 of the original DKIST image. The labeled panels below show, from left to right, the DKIST data degraded to the equivalent resolution of GREGOR, the SST, and the DST, respectively. This figure shows the effect of spatial resolution on the observed structure of BPs for both BP chains and isolated features.

coefficient (A. S. Monin & A. M. Iaglom 1975), K, is calculated using the diffusion index. The diffusion coefficient indicates the efficiency of BP dispersal; therefore, these metrics are useful to understand BP dynamics and field dispersal at these scales.

4. Results

4.1. Bright Point Area

Across the DKIST data, 12,486 individual BPs were identified. Adjusting for differences in the field of view and the duration of the observations between these data and the data used in P. H. Keys et al. (2011; DST data analyzed with the same algorithm), ∼2.7 times more BPs were identified within this dataset. The increase in numbers detected is due to a greater number of smaller features identified as a result of the superior resolving power of DKIST.

The area distribution of the BPs identified is shown in Figure 4 (black line). The peak of the distribution corresponds to an area of ∼2300 km^2, which would give an effective diameter for a BP (assuming a circular geometry) of 54 km. It should be clear from Figure 1 that BPs do not typically have a circular geometry, with extended chains being somewhat common and smaller BPs resembling more of a "raindrop" shape. However, we report the equivalent diameter here, as it is a metric that is often reported in the literature with regards to BP areas (e.g., D. Utz et al. 2009). A study of high-resolution MHD simulations by C. L. Peck et al. (2019) found BPs range from circular shapes to elongated sheets, with most structures having a width of ∼70 km.

The peak in area here is substantially lower to those reported previously. To explore the reasons behind this further, as described above, the spatial resolution of the data was degraded to match that of three other facilities/instruments (GREGOR, SST, and DST), while the temporal resolution was kept the same. The same process of tracking the data was performed on the degraded data, identifying 3382, 2937, and 2849 BPs in the GREGOR, SST, and DST data, respectively. The purpose of this was to ascertain how the area distribution and characteristics varied across the different facilities to confirm whether the variations are solely due to the resolving power of DKIST or if there is another reason for the discrepancy. By degrading the existing DKIST data, we can

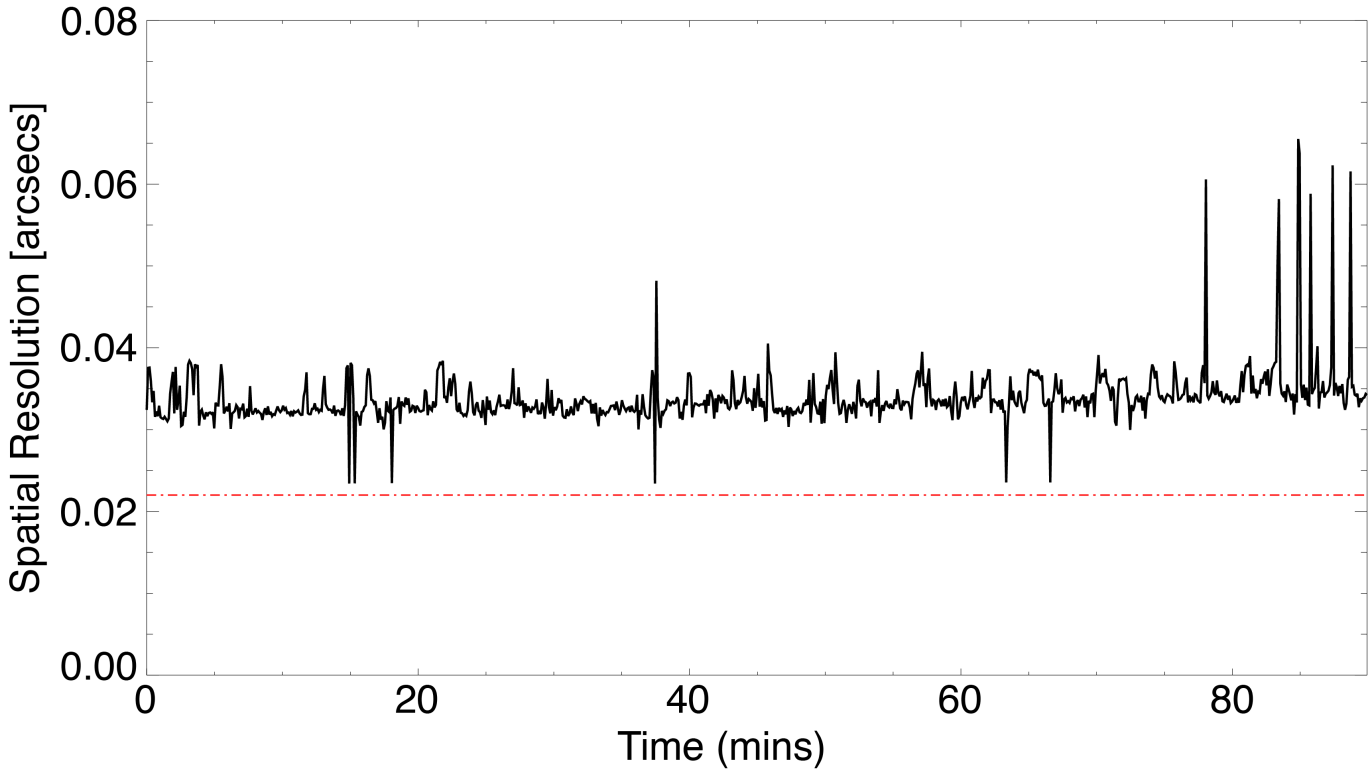

Figure 3. The variation of spatial resolution over the course of observations. The spatial resolution is estimated with Fourier techniques, outlined in C. Beck et al. (2007). The zero time is the first frame of the observations obtained at 17:46 UT on 2022 May 26. The plot is limited to images prior to an AO lock-point jump, which occurs at about 90 minutes into the sequence. The drop in image quality prior to the loss of the AO lock is evident in the plot. The red dotted–dashed line indicates the theoretical diffraction-limited resolution of the data acquired. The average spatial resolution for the sequence is 0.″034 ± 0.″007.

obtain a like-for-like comparison of the identified features in the images. That is, the same BPs should be contained in the data; only the change in spatial resolution should result in any differences in the identified BP characteristics.

Figure 4 shows the effect of the spatial resolution on the BP area distributions. The dotted–dashed green, dashed orange, and dot–dotted–dashed blue lines show the corresponding distributions for the data degraded to the resolutions of GREGOR, the SST, and the DST, respectively, while the dotted lines correspond to the log-normal fits for the associated data. The peaks for the distributions occur at approximately 13,700 km^2, 25,700 km^2, and 26,200 km^2 for the GREGOR, SST, and DST data, respectively. In a circular geometry this corresponds to diameters of around 132 km, 181 km, and 183 km for the GREGOR, SST, and DST data, respectively.

4.2. Varying Spatial Resolution

Having estimated the spatial resolution in each frame (see Section 3), we then used these values to filter the area estimates in each frame, so that only BPs resolvable in a given frame are considered. To do this, the spatial resolution estimate in a given frame was used to estimate the smallest resolvable pixel dimensions for a BP within that frame. Any BP which fell below that limit in the given frame was removed from the sample, as it was deemed unresolvable due to seeing, regardless of whether the algorithm was able to identify a feature of interest previously. This meant that seeing variations could be accounted for when determining the area distribution of the BPs. The resulting distributions can be seen in Figure 5. The peak of this distribution is around 4800 km^2, which corresponds to a diameter of 78 km when assuming a circular geometry. This is still significantly lower than previously reported area distributions. It should also be reiterated that the technique used to estimate the spatial resolution has the potential to overestimate the true spatial resolution.

Extending this analysis further, the spatial resolution estimates were used to isolate the area distributions for the best frames. As shown in Figure 3, there were six frames with a resolution better than 0.″026. From these six frames, 828 BPs were identified. The area distribution of BPs from these best frames was seen to match closely with the DKIST area distribution shown in Figure 4, with a peak at 2100 km^2.

4.3. Bright Point Dynamics

As well as establishing the area of the BPs, the tracking algorithm recorded the location of the BPs in each frame in which they were identified. This enabled analysis of the dynamic properties of BPs in the data (i.e., transverse velocities, lifetimes, and diffusion characteristics). Again, this was performed for both the DKIST data and the data degraded to the resolutions of GREGOR, the SST, and the DST. The distributions of velocities across the datasets are given in Figure 6.

The distribution of velocities for the DKIST data appears to have a sharper peak and a narrower tail, with few BPs displaying higher velocities. A greater number of higher-velocity BPs are detected in the degraded datasets. The peak of the distribution for the DKIST data occurs at approximately 0.83 $km\,s^{-1}$. The peaks for the degraded datasets appear at roughly the same velocity of 1.25 $km\,s^{-1}$, although the GREGOR data have a slightly broader peak than the SST

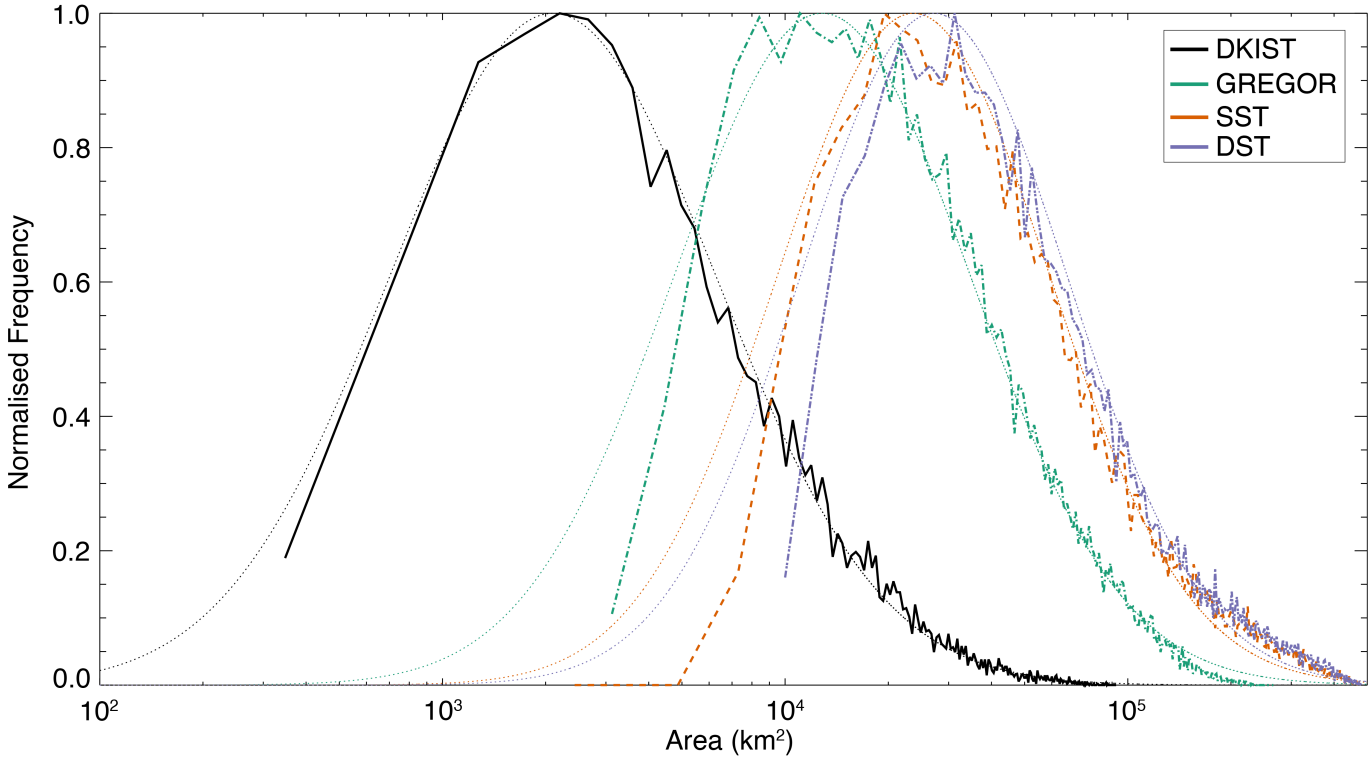

Figure 4. The area distribution of BPs identified in the datasets. The solid black line represents the original DKIST data, while the dotted–dashed green, dashed orange, and dot–dotted–dashed blue lines represent the area distributions for data degraded to the resolution of GREGOR, SST, and DST, respectively. The dotted lines indicate the corresponding log-normal fits for each of the distributions. The peaks of the distributions occur at approximately 2300 km^2, 13,700 km^2, 25,700 km^2, and 26,200 km^2 for the DKIST, GREGOR, SST, and DST data, respectively.

and the DST datasets. The shapes of the distributions somewhat mirror those of the area distributions. The results across all datasets are consistent with previous studies of BP velocity distributions (P. H. Keys et al. 2011).

Similar to the issues discussed in Section 4.2, variations in spatial resolution affect the estimated velocities, since the ability to resolve BPs varies with resolving power. Again, the variable spatial resolution is accounted for in the velocity estimates for the BPs in a manner similar to that outlined in Section 4.2. The results are shown in Figure 7. Accounting for the spatial resolution in each frame broadens the velocity distribution of the DKIST BPs and moves the peak of the distribution to a slightly larger velocity value. The distribution now matches the distributions for the degraded data, particularly with regard to the shape of the distribution. The mean BP velocity for the filtered data is found to be 2.28 ± 0.58 km s^{-1}, which again is similar to the degraded datasets.

The diffusion index, γ, is a useful metric for determining whether the BP motions follow normal diffusion ($\gamma = 1$), or are superdiffusive ($\gamma > 1$) or subdiffusive ($\gamma < 1$). The value for γ for the DKIST data is 1.22 ± 0.41, increasing to 1.24 ± 0.43 when accounting for seeing using the spatial resolution estimates of the frames. For the degraded datasets γ is estimated as 1.40 ± 0.58, 1.52 ± 0.69, and 1.55 ± 0.73 for the GREGOR, SST, and DST data, respectively. This is slightly higher than the DKIST results, but still within the associated errors, and implies that the BPs follow a superdiffusive regime.

The diffusion coefficient, K, indicates the efficiency of the BP dispersal. For the DKIST data, K is 30 ± 18 $km^2\,s^{-1}$, increasing to 74 ± 47 $km^2\,s^{-1}$ after applying spatial resolution filtering. For the degraded datasets, K is estimated as 98 ± 55 $km^2\,s^{-1}$, 142 ± 83 $km^2\,s^{-1}$, and 144 ± 83 $km^2\,s^{-1}$ for the GREGOR, SST, and DST data, respectively.

It should be noted that the estimated average lifetime of the BPs was established to be 95 ± 29 s, 97 ± 32 s, 98 ± 33 s, and 97 ± 33 s for the DKIST, GREGOR, SST, and DST data, respectively. The values for the lifetimes are in agreement across all the datasets.

More prominent variations appear when considering the longest-lived BPs detected. For the DKIST data, the maximum BP lifetime was found to be ~22 minutes, whereas for the GREGOR, SST, and DST datasets, the longest lifetimes were ~35 minutes. These do not correspond to the same features, though they correspond to BPs within the same spatial region (i.e., around $-10''$ to $0''$ in x and $0''$ to $10''$ in y in Figure 1). The average velocities across their lifetimes for these longer-lived BPs are below 0.5 km s^{-1} for all four datasets, suggesting that longer-lived BPs are less dynamic. Similar behavior with regards to lifetime and velocity has been reported in the literature (L. P. Chitta et al. 2012; P. H. Keys et al. 2014; G. Berrios Saavedra et al. 2022). It should be noted that degradation was performed on the spatial dimensions and not the temporal scale. Therefore, any differences with respect to lifetimes are due to the classification of BPs at lower spatial resolutions by the code, as opposed to being the result of poorer temporal sampling.

5. Discussion

5.1. Bright Point Areas

The area distribution is well fit with a log-normal distribution, as seen in Figure 4 (dotted black line). Such distributions have been reported previously for BPs

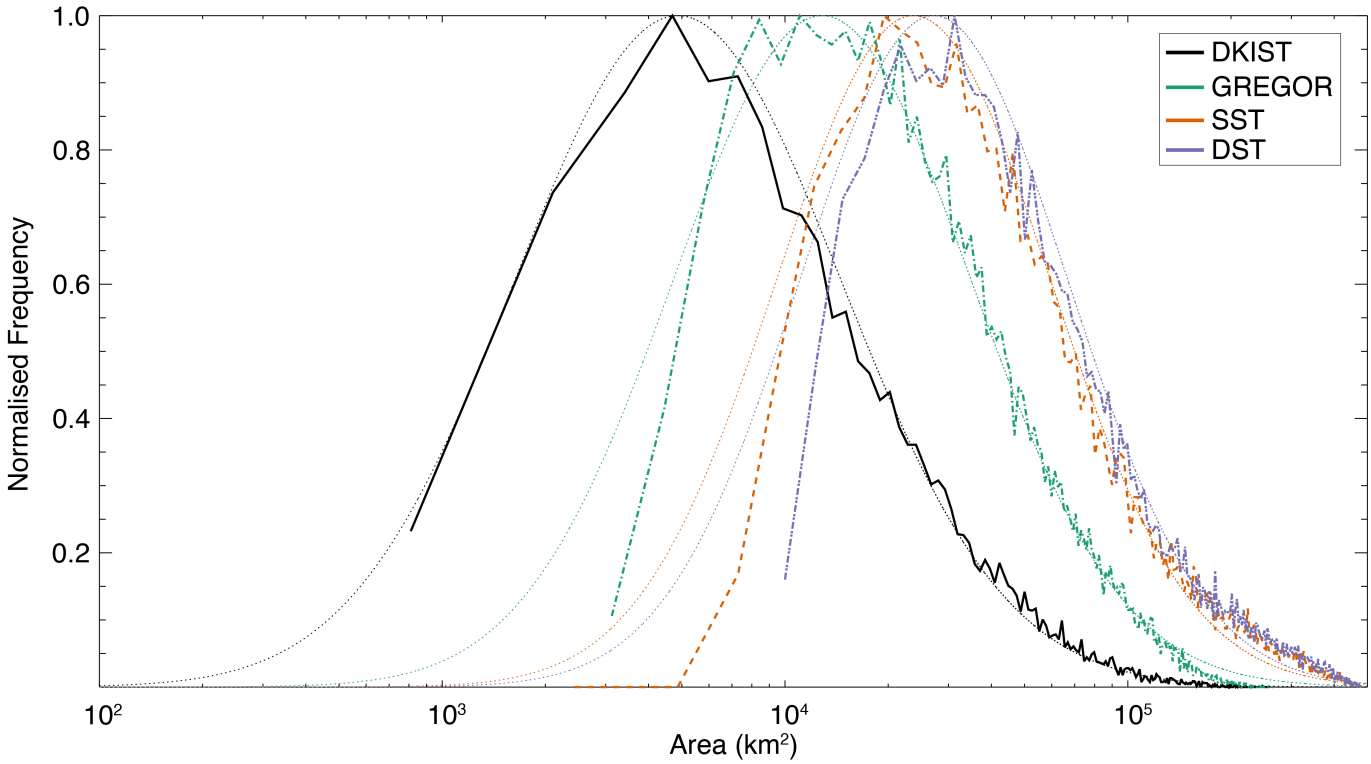

Figure 5. The area distribution of DKIST BPs adjusted for variations in seeing across the dataset. The filtered DKIST distribution is displayed with the solid black line, while the associated DKIST data degraded to the resolution of other facilities, as shown in Figure 4, are included here again for reference. As before, the dotted lines show the associated log-normal fits for the distributions. Accounting for the variable seeing conditions across the dataset shifts the peak location to around 4800 km^2. The peak of the distribution occurs at a smaller area than those of the degraded datasets; however, accounting for seeing returns a distribution shape that matches better with those previously reported in the literature for facilities with reduced spatial resolution. The effects of seeing are pronounced with the DKIST data, so care must be taken in analyzing results obtained with these data.

(P. J. Crockett et al. 2009; P. H. Keys et al. 2014; G. Berrios Saavedra et al. 2022), so this is not unexpected. However, the distribution for the area in the DKIST data has a peak at a smaller area (∼2300 km^2) and has a sharper tail than previous observations (e.g., a mean peak in area of 27,000 km^2 as reported by P. H. Keys et al. 2014). The change in location of the peak is perhaps not unexpected. The theoretical diffraction-limited resolution is substantially better with DKIST than with any other facility. This would indicate that the average BP detected in DKIST data is smaller than at other facilities, and that smaller features were perhaps not resolved adequately previously. Furthermore, a sharper tail in the distribution would suggest that there are fewer longer chains of BPs than previously observed. Again, this is perhaps not unexpected, as the superior spatial resolution afforded by DKIST may be able to distinguish separate entities in larger groups of BPs which perhaps were unresolved previously.

The degradation of the data to lower spatial resolutions, as expected, resulted in changes to the average sizes of the BPs. The distributions still follow log-normal forms quite well, however the peaks of these distributions occur at larger area values (13,700 km^2, 25,700 km^2, and 26,200 km^2 for the GREGOR, SST, and DST data, respectively), consistent with the lower spatial resolutions of these facilities. That is, at lower resolutions, the peak of the distribution is pushed to higher values. In addition, the tail of the distribution is broader for these degraded images.

These results are not unexpected; however, the difference in the area peak values obtained with each dataset does not correspond solely due to the change in scaling of the spatial resolution. That is, the shift in the location of the peak is not proportional to the variation in pixel scale. Therefore, with the change in spatial scale, additional factors must influence both the location of the peak and the shape of the distribution in the degraded data.

To explore this further, we looked closer at the detected BPs across the datasets to identify any commonalities that could explain some of the observed variations. One of the most common issues leading to larger BPs was a direct consequence of the spatial resolution, in that features close to each other were identified as one single entity as opposed to separate features. This is not only a case of smaller features being missed, as one might expect; rather, it is a scenario in which the sizes of BPs that should be easily distinguishable in the degraded data are conflated with neighboring pixels of smaller features.

An example of this can be seen in Figure 8, where a region is identified within a red box of BPs in close proximity to each other. A red line indicates one of the intensity cross-cuts used to identify the BP boundary locations. This direction was chosen to illustrate the effects of intensity thresholding at various spatial resolutions. The middle panels of the figure show the BPs identified in each of the datasets, with the cyan contours indicating the boundaries identified by the algorithm for each particular dataset. The final panels on the right show the corresponding intensity curves used by the algorithm to identify the BP boundaries for the red line shown in the leftmost panel.

This figure clearly shows that the algorithm identifies the same feature differently depending on the spatial resolution.

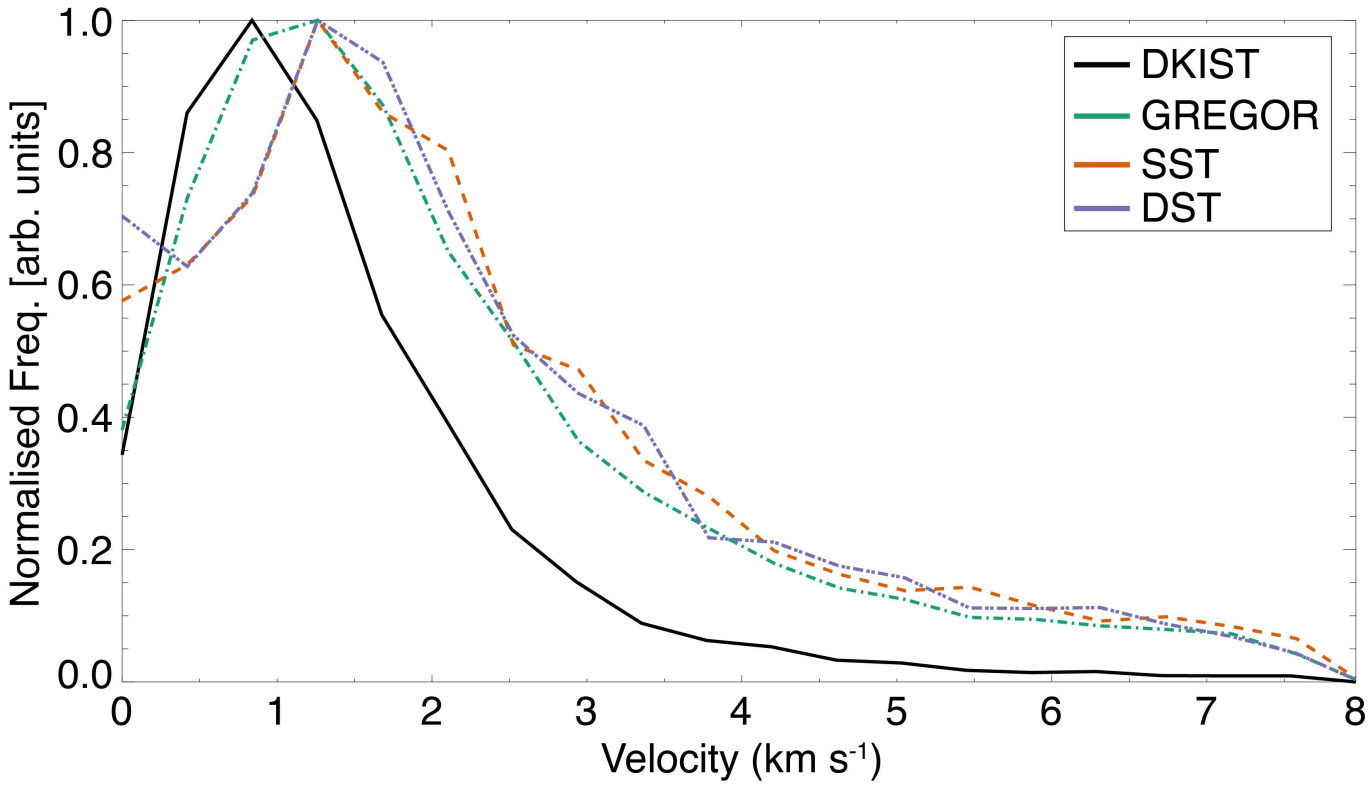

Figure 6. The velocity distributions of BPs identified in DKIST data and the DKIST data degraded to the resolution of GREGOR, the SST, and the DST. The solid black line represents the original DKIST data, while the dotted–dashed green, dashed orange, and dot–dotted–dashed blue lines represent the area distributions for data degraded to the resolution of GREGOR, SST, and DST, respectively. The peaks of the distributions occur at approximately 0.83 km s^{-1} for DKIST and 1.25 km s^{-1} for the degraded datasets. The mean BP velocities are 1.60 ± 0.41 km s^{-1}, 2.30 ± 0.64 km s^{-1}, 2.44 ± 0.68 km s^{-1}, and 2.36 ± 0.66 km s^{-1} for the DKIST, GREGOR, SST, and DST data, respectively.

For the DKIST data, two features are identified: a larger feature within the middle of the panel, with a smaller feature identified to the top right of the larger feature. For the GREGOR data, the larger feature is identified, but the smaller feature to the top right is missed. For both the SST and DST datasets, the larger feature and the smaller feature to the top right are identified as one individual feature.

The intensity curves for each dataset show how the algorithm reaches these conclusions. The algorithm looks for turning points at the edges of the BPs as the points at which there is a transition from brighter BP pixels to the darker surrounding intergranular lane pixels. To distinguish BPs from other small bright features, the algorithm uses a gradient threshold to separate real features from possible false detections. BPs will have a steeper intensity gradient going from the intergranular lanes to the center of the BP, as the intensity at the center of the BP is above the quiescent level of the surrounding granules.

For both the SST and DST data in the example shown in Figure 8, the reduced spatial resolution results in the intensity in the region between the two features being "blended." This acts to reduce the intensity gradient between the two features, so the algorithm does not detect them as individual features. As such, a single entity is identified, increasing the total area of that particular BP. Furthermore, for this particular case, the smaller feature to the top right has a double peak in intensity, albeit not sufficient to be identified as separate features in any dataset. An effect of the reduction in spatial resolution here is that this double peak is not seen in the SST and DST data, though it is observed in both the DKIST and GREGOR data.

For the GREGOR data, there is sufficient resolution to detect the boundary of the larger feature as the algorithm can pick out the turning point around 400 km across the slice. However, for the smaller feature to the top right, there are insufficient pixels for the code to identify the left side of this smaller feature. As the algorithm cannot establish the boundary here, the BP is not identified. Hence, for the GREGOR data, the larger feature has a more accurately determined boundary, and therefore area component. Nevertheless, the smaller feature is not detected, and so smaller components of the BP area distribution are missed.

This is the most common variation in boundary determination across the datasets. Smaller features are either not resolved at all at lower resolutions or not detected as the spatial resolution effectively "blurs" the boundaries between BP pixels and the intergranular lanes, and therefore the gradient of features is insufficient to identify a BP. As outlined above, numerous cases are seen in which nearby features are conflated with larger features at lower spatial resolution.

An additional scenario affecting the BP area distribution occurs for larger-scale features. This predominantly affects larger features identified in DKIST data and possibly explains the sharp tail in the DKIST distribution at larger area values. For larger BPs, like those found in BP chains, the algorithm occasionally misses longer BPs entirely as it considers them as false detections. This scenario occurs for BPs whose centers are not sufficiently greater in intensity than the quiescent background level (i.e., only marginally brighter than granules). This results in the gradient in certain directions across a BP not

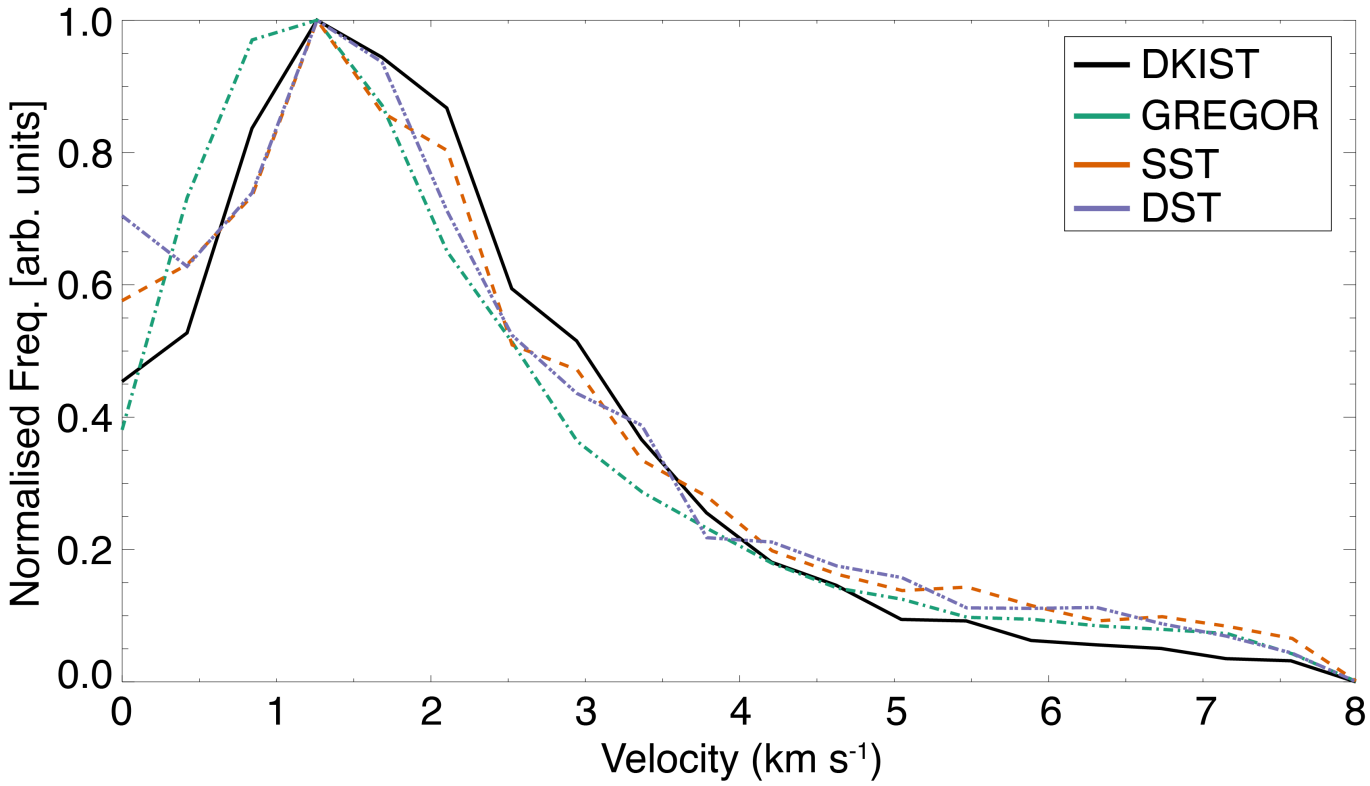

Figure 7. The velocity distribution of BPs identified in DKIST data adjusted for variations in seeing across the dataset. The filtered DKIST distribution is displayed with the solid black line, while the associated DKIST data degraded to the resolution of other facilities, as shown in Figure 6, are included here again for reference. Accounting for fluctuations in seeing broadens the distribution and shifts the peak so that the DKIST velocity distributions match closer to those of the degraded datasets. The mean velocity for the filtered DKIST data is 2.28 ± 0.58 km s^{-1}.

being sufficient for the code to identify it as a feature. Instead, the algorithm treats it similarly to an exploding granule and discards the feature.

Another issue with longer BPs occurs with the DKIST data, where the algorithm segments longer chained features into smaller components, whereas for lower-resolution datasets these chains are identified as singular features. This again acts to increase the number of smaller features detected in DKIST data. This scenario can be slightly more challenging to accurately interpret, and essentially comes down to that somewhat subjective definition of what constitutes a BP and where its boundaries lie; that is, the interpretation that these chains consist of individual features sufficiently close enough together to appear as a single long feature could be justified. As such, with the resolution of DKIST the algorithm detects these as individual smaller features. However, the intensity of the pixels between these individual bright centers does not return to levels similar to intergranular lane pixels. This suggests that substantial flux remains between the bright centers. Therefore, it could be argued that these features are one entity with multiple bright centers representing regions of greater magnetic flux. This is clearly distinct from the scenario shown in Figure 8, where two features are close together and the intensity drops nearly to the level of the intergranular lanes, which would be indicative of distinct features. Ultimately, this comes down to how the boundary of the BP is defined. Further work is needed here to explicitly determine the internal magnetic structures of these longer chains that have been segmented, to support the discussion of whether they can be treated as individual features or one single chain. Unfortunately, there is insufficient data to determine the internal magnetic fields associated with these chains for these observations, and high-spatial-resolution and high-temporal-resolution 2D polarimetric data would be needed to further analyze these chains.

The issue with longer elements may be addressed by better techniques, e.g., deep learning techniques (Y. Yang et al. 2019; L. Xu et al. 2021). However, these techniques are often supervised deep learning methods, and so require a large volume of annotated data (H. Bai et al. 2023); therefore, the issue of the interpretation of groups and chains may still pose a challenge. To reiterate, care must be taken when interpreting longer elements to determine whether these features should be interpreted as individual features or a conglomeration of several features. A suitable observing sequence with high-spatial-resolution polarimetric data would be needed to confirm which interpretation is correct.

Another possible explanation for the variations observed between the DKIST results and the degraded datasets could come from the work of G. Berrios Saavedra et al. (2022), where the authors analyzed BPs in GREGOR and Hinode datasets and found the usual log-normal distribution for BP areas. However, the authors report that the log-normal distribution is composed of two separate components, interpreted as two different populations of BPs from network and intranetwork flux elements. Interestingly, for their GREGOR dataset, the authors report a mean BP area of 5700 km^2 for the lower area component and a mean of 16,000 km^2 for the larger area component. The DKIST distribution may be sampling this lower area component. It should be noted that the field of view

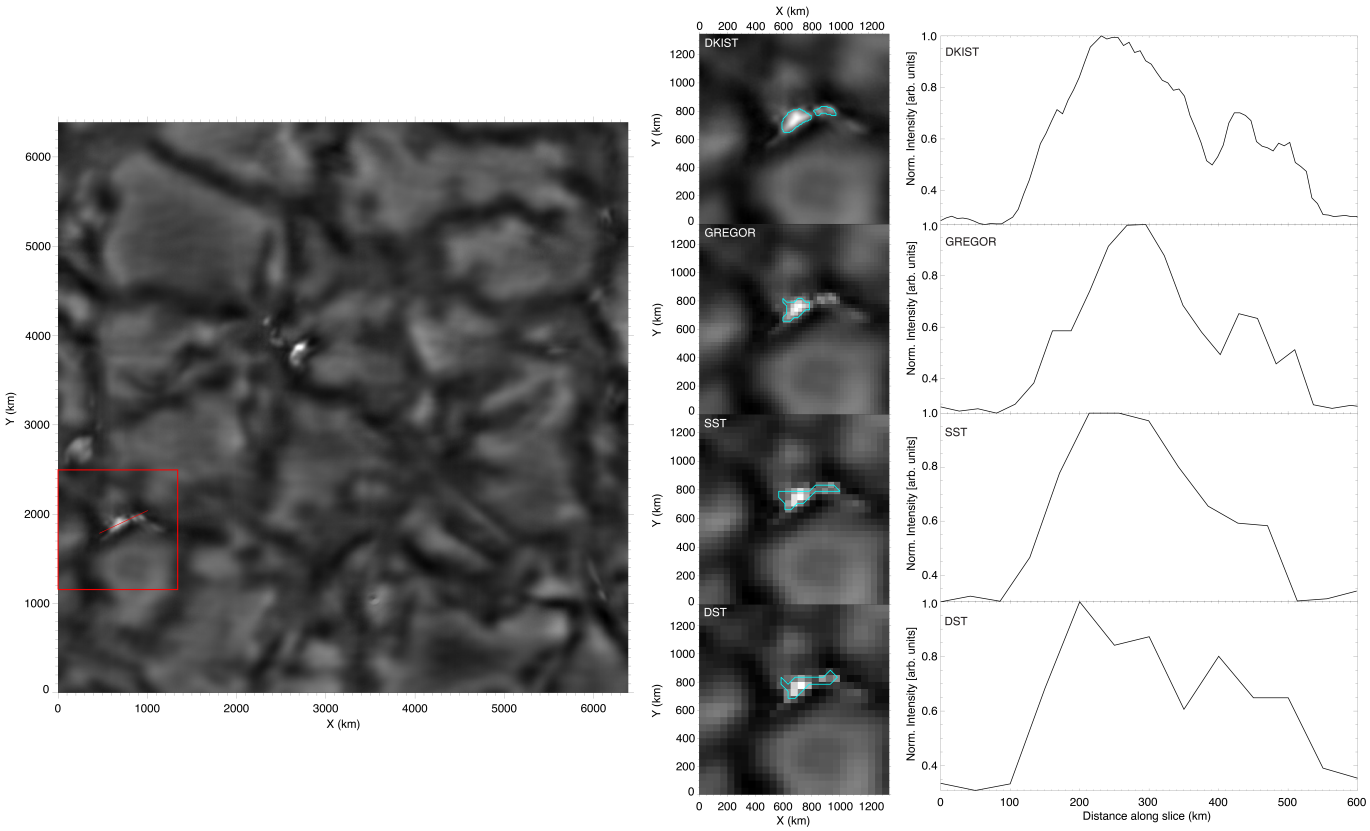

Figure 8. Sample images showing the determination of BP boundaries across the different datasets. The image on the left-hand side shows a slightly expanded field of view of the region for context. The red box indicates the region displayed in the middle panels, while the red line across the BP indicates the position of the cross-cut used in the intensity plots in the rightmost panels. The middle panels indicate the appearance of the BPs across the different datasets, from top to bottom, going from highest to lowest spatial resolution. The cyan colored contours indicate the detected boundary locations of the BPs. The panels to the right of these intensity images give sample light curves from the cross-cut of the BPs at the various resolutions. It should be noted that, in this case, for DKIST data the code identified two independent BPs, for GREGOR data the code identified the larger BP but missed the smaller BP, and both BPs are identified as a single entity with the SST and DST data.

of VBI is slightly larger than the typical widths of a supergranular cell (T. Roudier et al. 2014; M. Noori et al. 2019). It is possible, then, that this particular observed region preferentially samples the center of a network cell, and so our sample of BPs is predominantly intranetwork BPs that produce this lower area component.

5.2. Spatial Resolution

One issue that could affect the area distribution reported for the DKIST data is the variable seeing conditions across the dataset. Seeing obviously is an issue with ground-based observations, and can cause issues for small-scale features such as BPs as they are close to the resolution limit. Seeing conditions were relatively good across this dataset, although there were some fluctuations (Figure 3).

When accounting for seeing conditions by filtering detections below the smallest resolvable pixel dimensions in a given frame, the peak of the area distribution for the DKIST BPs was revised to 4800 km^2. This is similar to the values for the lower area components reported by G. Berrios Saavedra et al. (2022). The peak for the filtered area is approximately 2.1 times larger than that using the spatial sampling of the data. The distribution can again be fitted well with a log-normal distribution. The tail of the distribution is also less sharp than the original distribution.

It is clear that care must be taken when analyzing the spatial characteristics of small-scale elements such as BPs, particularly for data susceptible to seeing fluctuations. Small fluctuations can have a large impact on small features (V. Abramenko et al. 2010; T. L. Riethmüller et al. 2014; G. Berrios Saavedra et al. 2022). Looking at the adjusted distribution, it is clear that the distribution of area values is larger than initially estimated, although still lower than the values estimated with facilities with lower spatial resolutions. This distribution is likely to still estimate lower values for areas due to the issues mentioned in Section 5.1; that is, longer chains are misinterpreted as false detections and excluded, as well as longer elements being segmented by the algorithm into smaller components. However, the peak is still consistent with the lower component reported by G. Berrios Saavedra et al. (2022). This suggests that, even after adjusting for the effects of seeing, the superior resolving power of DKIST coupled with the field of view of VBI means that smaller intranetwork BPs are adequately resolved and preferentially sampled with these observations.

The results of D. Kuridze et al. (2025) are relevant when considering the area distribution and size of the BPs. Here, the authors utilized the field-sampling mode of the VBI to create a mosaic (with 3×3 tiles) of a larger field of view of the photosphere, at the cost of temporal resolution. The authors image faculae off disk center ($\mu \approx 0.85$) and report spatial resolutions in the range $0\farcs022 - 0\farcs030$, which was determined

based on the smallest resolved structures observed in the data. Compared with MURaM simulations (M. Rempel 2014), the authors interpret striations near granular edges as due to the magnetic flux density within the lanes creating a Wilson depression, and report widths in the range of 20–50 km for the eight striae that were sampled.

Faculae can be interpreted as BPs viewed at an angle (M. Carlsson et al. 2004). Therefore, the results with regards to the width of the striations found by D. Kuridze et al. (2025) appear consistent with the results we present here for BP diameters (particularly with our original unfiltered results of 54 km) at the upper range of their reported widths. More details are needed to evaluate their estimation of the spatial resolution, as there is insufficient information as to how this was performed. There is a potential selection bias introduced when considering the smallest resolved structures, which the Fourier technique should avoid. This, coupled with an average r_0 of 12.2 cm for these data (which is comparable to the data presented here), suggests that the spatial resolution of their data could be larger than reported. Nevertheless, the MURaM simulations presented in the work of D. Kuridze et al. (2025) support striations of these widths and possibly smaller. This highlights the challenges in interpreting the scale of these features and the role of simulations in supporting observational work.

Regardless, the results for the area distributions confirm that smaller-scale elements than previously reported are observable with DKIST, highlighting the necessity of DKIST data to accurately classify this smaller component of the BP distribution. This is further highlighted when limiting the area distribution to the six best frames in the dataset, which resulted in a distribution similar to our original unfiltered area distribution, suggesting that these smaller features are more readily identified in DKIST data. Previous work looking at area distributions likely had systematic errors in the reported statistics as a result of the resolving power. However, the results indicate that facilities such as GREGOR should be able to adequately sample these smaller-scale features.

5.3. Bright Point Dynamics

The velocity characteristics were largely similar between the original DKIST data and the DKIST data degraded to the resolutions of GREGOR, the SST, and the DST. The peak in velocity occurs at 0.83 km s^{-1} for DKIST and 1.25 km s^{-1} for the degraded datasets, as seen in Figure 6. The degraded datasets have a longer tail of higher-velocity BPs. This results in a higher mean BP velocity for the degraded data (2.30 ± 0.64 km s^{-1}, 2.44 ± 0.68 km s^{-1}, and 2.36 ± 0.66 km s^{-1} for the GREGOR, SST, and DST data, respectively) in comparison to the DKIST data (1.60 ± 0.41 km s^{-1}). These values are in agreement with results from the literature (e.g., with peaks found around 1–2 km s^{-1}; D. Utz et al. 2010; P. H. Keys et al. 2011; L. P. Chitta et al. 2012; to name a few).

The differences in velocity characteristics at higher velocities are partially due to the issues outlined in Section 5.1, where BPs in close proximity can be detected as a single element at lower spatial resolutions (see Figure 8). In these scenarios, it is possible that between frames the BPs in close proximity separate enough to be detected as distinct entities, shifting the barycenter of the original BP. Similarly, if two separate entities are close enough to each other that in a subsequent frame they are identified as a single object, this can be sufficient to shift the barycenter by a few pixels, registering as a large transversal velocity excursion that acts to artificially broaden the velocity distribution at higher velocity values. These issues will be exacerbated as the reduced spatial resolution of the degraded datasets will have a higher degree of uncertainty associated with the spatial dimensions of the pixels. This is further compounded by variable seeing conditions, where a drop in image quality due to atmospheric variations can "smear" the boundaries of two features in close proximity, causing them to be identified as a single entity in the frame affected by poorer seeing conditions.

Figure 7 shows the effects on the velocity distribution when adjusted for the effects of seeing. Filtering the data to remove features that are not adequately resolved due to seeing variations, the peak of the distribution shifts to a slightly higher velocity ($\sim$1.18 km s^{-1}) and becomes coincident with the peaks of the degraded datasets. The shape of the DKIST distribution broadens with this adjustment, with the mean velocity changing to 2.28 ± 0.58 km s^{-1}. This can be interpreted as the seeing-induced reduction in spatial resolution affecting the sample of resolvable BPs. This results in larger BPs in the sample, which are susceptible to errors in transverse velocity estimates due to barycenter fluctuations. This further results in a shift of the peak in the velocity distribution to higher velocities and a broadening of the distribution, with more higher-velocity BPs reported. The true velocity distribution of the BPs may be lower than reported in the literature (similar to the unfiltered DKIST results); however, data with more consistent seeing conditions and a resolution close to the diffraction limit of DKIST are needed to confirm this. With the present data, the velocity characteristics appear consistent with previous work.

The value for γ was estimated as 1.22 ± 0.41 for the DKIST data (1.24 ± 0.43 for the seeing-filtered DKIST data), and as 1.40 ± 0.58, 1.52 ± 0.69, and 1.55 ± 0.73 for the GREGOR, SST, and DST data, respectively. This implies that the BPs in the DKIST data are superdiffusive. For a BP's transverse motion, this appears as a random walk pattern with occasional Lévy flights. This is consistent with previous work on the diffusion of BPs (F. Giannattasio et al. 2014; P. H. Keys et al. 2014; Y. Yang et al. 2015; F. Giannattasio et al. 2019).

The enhanced superdiffusive motions in the degraded datasets is likely due to shifts in barycenter positions when BPs in close proximity are identified as a single feature in one frame and as separate in the next. This is exacerbated at lower spatial resolutions, as these features may be identified erroneously as one entity. This is reflected in the fact that the γ value is higher at lower resolutions (i.e., for the degraded datasets), which implies more Lévy flights for BPs in the lower-resolution datasets. Previous work with DST data (P. H. Keys et al. 2014) found a γ value of $\sim$1.2, so it is possible that the BPs in this particular observation are slightly more superdiffusive than previously observed. This is supported by the fact that the velocity distribution is more elevated than in the result of P. H. Keys et al. (2014), who found mean velocities in the range $\sim$0.6–0.9 km s^{-1}.

Values for K were estimated as 30 ± 18 km^2 s^{-1} for the DKIST data (74 ± 47 km^2 s^{-1} for the seeing-filtered DKIST data) and as 98 ± 55 km^2 s^{-1}, 142 ± 83 km^2 s^{-1}, and 144 ± 83 km^2 s^{-1} for the GREGOR, SST, and DST data, respectively. The values here are consistent with those found in the literature (T. E. Berger et al. 1998; H. J. Hagenaar et al. 1999; V. I. Abramenko et al. 2011; S. Jafarzadeh et al. 2017;

L. Bellot Rubio & D. Orozco Suárez 2019; F. Rincon et al. 2025). The value for the original unfiltered DKIST data is somewhat lower than the other datasets. Values for K for BPs are typically below $\sim$300 km^2 s^{-1}, with many values reported below $\sim$100 km^2 s^{-1} (R. Cameron et al. 2011; L. P. Chitta et al. 2012; Y. Yang et al. 2015), and a reported value as low as 12 km^2 s^{-1} (V. I. Abramenko et al. 2011). The lower values obtained with BPs is due to the fact that their motion and transport is governed by shorter-lived, smaller-scale structures such as granules as opposed to supergranular cells (F. Rincon et al. 2025).

The variation in K observed between the original DKIST data and the degraded datasets is not unexpected. It has been shown for superdiffusive motions ($\gamma > 1$), K is directly proportional to both the temporal and spatial scales (V. I. Abramenko et al. 2011), with decreasing values for decreasing temporal and spatial scales. Therefore, as the spatial resolution decreases, the value of K will increase, which is what is reported here.

The average lifetimes were estimated as 95 ± 29 s, 97 ± 32 s, 98 ± 33 s, and 97 ± 33 s for the DKIST, GREGOR, SST, and DST data, respectively. The values are consistent with those obtained in previous studies of quiet-Sun BPs (P. H. Keys et al. 2011, 2014). This suggests that around 1.5 minutes is a typical average lifetime of BPs in the quiet Sun. Lifetimes may be larger on average for network BPs or BPs in the vicinity of an active region. This difference between isolated and nonisolated BP lifetimes has been reported by Y. Liu et al. (2018), with nonisolated BPs surviving on average around 1.5 times longer than isolated BPs. Future work will look to establish the variations associated with location within the network cell. Again, it should be noted that the field of view of VBI is slightly larger than the typical widths of a supergranular cell, so additional data would be required to classify BPs as network or internetwork. However, the average lifetimes we report are consistent across the DKIST data and the degraded datasets, and follow those in the literature.

6. Conclusions

Data from the newly commissioned DKIST were utilized to determine the characteristics of small-scale features (BPs) across the solar surface at the highest spatial resolutions currently achievable. This is the first analysis of the properties of BPs with DKIST, and the highest-resolution analysis of BPs ever performed.

The VBI instrument was used to obtain photospheric images of a quiet-Sun region at disk center with the G-band filter for around 90 minutes using the highest spatial sampling possible (0.″011 pixel^{-1}) with DKIST. Analysis of the images showed that the average spatial resolution of the data was around $0.''034 \pm 0.''007$, with a handful of frames obtained close to the diffraction limit, with a spatial resolution of 0.″023. The lowest-quality image in this dataset had an estimated spatial resolution of 0.″066. The data have an average r_0 value of 12.1 ± 3.1 cm and a range of 10.2–20.9 cm.

BPs are small-scale intensity enhancements that are often the manifestation of kilogauss magnetic fields observed between granules on the solar surface. An automated detection and tracking algorithm was employed to identify BPs across the dataset so that their properties could be analyzed. BPs were observed to have an average lifetime of 95 ± 29 s, consistent with previous studies. The BPs were found to have a log-normal velocity distribution with a peak at 0.83 km s^{-1} and a mean velocity of 1.60 ± 0.41 km s^{-1}, again consistent with previous work.

The BP areas were also determined, showing the biggest differences from previous work. The areas were found to have a log-normal distribution with a peak at 2300 km^2. This is somewhat lower than values found in previous studies (P. J. Crockett et al. 2010; P. H. Keys et al. 2014), although it is perhaps due to the lower area component seen in the literature (G. Berrios Saavedra et al. 2022). It is possible that the higher spatial resolution obtained with DKIST is able to resolve smaller features more readily. With this, the distribution was narrower than those seen previously, suggesting that smaller features were observed than in previous work, again highlighting that the lower area component was preferentially sampled. This is supported by the size of VBI's field of view, which is close to the scale of a supergranular cell. It is possible, then, that intranetwork BPs are preferentially sampled here, returning the lower area component reported by G. Berrios Saavedra et al. (2022).

To compare with previous results more readily, the DKIST data were degraded to match the resolutions of commonly used ground-based facilities, namely, GREGOR, the SST, and the DST. The same detection and tracking algorithm was applied to the degraded datasets. These datasets showed the same log-normal distributions for the area as the DKIST data, albeit with peaks at larger areas. The distributions from the degraded datasets matched well with area distributions reported previously for these facilities. It was observed that for the datasets with lower spatial resolution, frequently smaller groupings of BPs would be identified as a single entity, as there was insufficient resolving power to determine accurate boundaries. This acted to increase the number of larger features observed in these data. To obtain a more accurate picture of BP area distributions, the area estimates were adjusted for a seeing-induced reduction in spatial resolution in the images for the DKIST data by filtering out BPs that fell below the resolution limit in a given frame. This led to the area distribution shifting to slightly higher values, with the peak now found at 4800 km^2. The peak still falls well below that of the degraded examples, but is likely closer to the "true" distribution of the areas for this dataset. Furthermore, isolating the area distribution for the six best frames in the dataset returned a distribution similar to the original, unfiltered dataset, suggesting that smaller features are more readily identified in DKIST data. It may be that a dataset with more consistently excellent seeing throughout will exhibit this distribution with a peak at smaller areas.

The observed area distribution accuracy will only be improved with data with more consistent seeing for the duration, so that the images are close to the diffraction limit for the duration of the sequence. This would ensure that the BPs are sampled with consistently excellent spatial resolution, which is vitally important for features at this scale. If consistent quality across a sequence could be achieved, the limiting factor for resolving BPs for a telescope with the aperture width of DKIST would be the mean free path of a photon in the photosphere. Other techniques may be needed to interpret the structuring of longer chains of BPs, which are possibly underestimated with the current detection algorithm employed with DKIST data.

The velocities and lifetimes of the BPs were also analyzed with the degraded datasets. The average lifetimes of the BPs were consistent with the DKIST results and with previous studies. The velocity distributions for the degraded datasets were consistent with previous studies, and slightly elevated in comparison to the results from DKIST. The reason for this was due to the spatial resolution, as lower resolution introduces larger errors in the estimation of the transverse velocity. Similarly, some BPs had high velocities due to multiple features in close proximity. These BPs were first identified separately and then as a single entity between frames due to inadequate resolving power for the features. This meant that the barycenter of the BP could shift significantly between frames due to the change in size and shape of the larger BP, which then translated into a higher velocity estimate for these features. Therefore, care should be taken when considering BPs in groups (e.g., around a network boundary) when establishing their dynamic characteristics.

Features in close proximity can be an issue when dealing with feature tracking, and arise from the feature-classification process; that is, the way an algorithm defines the feature boundaries and classifies individual features between frames to track their continuation can never be completely accurate. Edge cases, such as features being identified as separate and then as one entity between subsequent frames, will add to the inaccuracy of the algorithm.

Similar issues exist for longer chains of BPs, where the constraints of the algorithm may oversegment features. This can be a challenging identification task, as it is open to interpretation and potential biases, e.g., whether dips in intensity across a chain are indicative of internal structuring of a singular entity or mark the boundaries for features in close proximity. Such image classification issues will exist with machine learning techniques as well (H. Bai et al. 2023), so other techniques and data may likely be necessary to understand the complex structuring of BP chains and closely packed groups.

Future work will look at signatures of BPs in other filters, and will make use of alternative techniques to understand the underlying structure of the BPs. This will aid our understanding of the magnetic field at the smallest scales and its coupling to higher regions of the solar atmosphere.

Acknowledgments

The authors are grateful to the anonymous referee for their suggestions to improve the manuscript. R.J.C., M.M., and D.B. J. acknowledge support from the Science and Technology Facilities Council (STFC) under grant Nos. ST/P000304/1, ST/T00021X/1, and ST/X000923/1. D.K.J.M. acknowledges a studentship funded by the Leverhulme Interdisciplinary Network on Algorithmic Solutions. R.E. acknowledges the NKFIH (OTKA; grant No. K142987) Hungary for enabling this research. R.E. is also grateful to the Science and Technology Facilities Council (STFC; grant No. ST/M000826/1) UK, PIFI (China; grant No. 2024PVA0043), and the NKFIH Excellence Grant TKP2021-NKTA-64 (Hungary). D.J.C. acknowledges partial support of this project from NASA grant Nos. 19-HSODS-004 and 21-SMDSS21-0047. The research reported herein is based on data collected with the Daniel K. Inouye Solar Telescope (DKIST), a facility of the National Solar Observatory (NSO). DKIST is located on land of spiritual and cultural significance to Native Hawaiian people. The use of this important site to further scientific knowledge is done so with appreciation and respect. NSO is managed by the Association of Universities for Research in Astronomy, Inc., and is funded by the National Science Foundation. Any opinions, findings, and conclusions or recommendations expressed in this publication are those of the author(s) and do not necessarily reflect the views of the National Science Foundation or the Association of Universities for Research in Astronomy, Inc. The observational data used during this research are openly available. Data availability statement: readers can access the DKIST data used in this study from the DKIST Data center Archive (https://dkist.data.nso.edu/) under proposal identifier pid_1_36. Finally, we wish to acknowledge scientific discussions with the Waves in the Lower Solar Atmosphere (WaLSA; https://www.WaLSA.team) team, which has been supported by the Research Council of Norway (project No. 262622), the Royal Society (award No. Hooke18b/SCTM; D. B. Jess et al. 2021), and the International Space Science Institute (ISSI Team 502).

Facilities: DKIST (T. R. Rimmele et al. 2020).

ORCID iDs

Peter H. Keys https://orcid.org/0000-0001-8556-470X
Ryan J. Campbell https://orcid.org/0000-0001-5699-2991
Dylan K. J. Magill https://orcid.org/0009-0000-6521-8842
Mateus A. Keating https://orcid.org/0009-0002-5370-8590
Mihalis Mathioudakis https://orcid.org/0000-0002-7725-6296
David B. Jess https://orcid.org/0000-0002-9155-8039
Damian J. Christian https://orcid.org/0000-0003-1746-3020
Arthur Berberyan https://orcid.org/0009-0009-8695-2558
Samuel D. T. Grant https://orcid.org/0000-0001-5170-9747
Shahin Jafarzadeh https://orcid.org/0000-0002-7711-5397
Marco Stangalini https://orcid.org/0000-0002-5365-7546
Robertus Erdélyi https://orcid.org/0000-0003-3439-4127

References

Abramenko, V., Yurchyshyn, V., Goode, P., & Kilcik, A. 2010, ApJL, 725, L101
Abramenko, V. I., Carbone, V., Yurchyshyn, V., et al. 2011, ApJ, 743, 133
Bai, H., Yang, P., Zhao, L., et al. 2023, ApJ, 956, 62
Beck, C., Bellot Rubio, L. R., Schlichenmaier, R., & Sütterlin, P. 2007, A&A, 472, 607
Bellot Rubio, L., & Orozco Suárez, D. 2019, LRSP, 16, 1
Berberyan, A., Keys, P. H., Jess, D. B., & Christian, D. J. 2024, A&A, 690, A363
Berger, T. E., Löfdahl, M. G., Shine, R. A., & Title, A. M. 1998, ApJ, 506, 439
Berrios Saavedra, G., Utz, D., Vargas Domínguez, S., et al. 2022, A&A, 657, A79
Buehler, D., Lagg, A., van Noort, M., & Solanki, S. K. 2019, A&A, 630, A86
Cadavid, A. C., Lawrence, J. K., & Ruzmaikin, A. A. 1999, ApJ, 521, 844
Cameron, R., Vögler, A., & Schüssler, M. 2011, A&A, 533, A86
Campbell, R. J., Keys, P. H., Mathioudakis, M., et al. 2023, ApJL, 955, L36
Campbell, R. J., Shelyag, S., Quintero Noda, C., et al. 2021, A&A, 654, A11
Carlsson, M., Stein, R. F., Nordlund, Å., & Scharmer, G. B. 2004, ApJL, 610, L137
Chitta, L. P., van Ballegooijen, A. A., Rouppe van der Voort, L., DeLuca, E. E., & Kariyappa, R. 2012, ApJ, 752, 48
Criscuoli, S., & Uitenbroek, H. 2014, A&A, 562, L1
Crockett, P. J., Jess, D. B., Mathioudakis, M., & Keenan, F. P. 2009, MNRAS, 397, 1852
Crockett, P. J., Mathioudakis, M., Jess, D. B., et al. 2010, ApJL, 722, L188
Cubas Armas, M., & Fabbian, D. 2021, ApJ, 923, 207
de Wijn, A. G., Casini, R., Carlile, A., et al. 2022, SoPh, 297, 22
de Wijn, A. G., Stenflo, J. O., Solanki, S. K., & Tsuneta, S. 2009, SSRv, 144, 275
Giannattasio, F., Consolini, G., Berrilli, F., & Del Moro, D. 2019, ApJ, 878, 33

Giannattasio, F., Stangalini, M., Berrilli, F., Del Moro, D., & Bellot Rubio, L. 2014, ApJ, 788, 137
Hagenaar, H. J., Schrijver, C. J., Title, A. M., & Shine, R. A. 1999, ApJ, 511, 932
Jafarzadeh, S., Cameron, R. H., Solanki, S. K., et al. 2014, A&A, 563, A101
Jafarzadeh, S., Solanki, S. K., Feller, A., et al. 2013, A&A, 549, A116
Jafarzadeh, S., Solanki, S. K., Cameron, R. H., et al. 2017, ApJS, 229, 8
Jess, D. B., Jafarzadeh, S., Keys, P. H., et al. 2023, LRSP, 20, 1
Jess, D. B., Keys, P. H., Stangalini, M., & Jafarzadeh, S. 2021, RSPTA, 379, 20200169
Jess, D. B., Mathioudakis, M., Christian, D. J., Crockett, P. J., & Keenan, F. P. 2010a, ApJL, 719, L134
Jess, D. B., Mathioudakis, M., Christian, D. J., et al. 2010b, SoPh, 261, 363
Keys, P. H., Mathioudakis, M., Jess, D. B., Mackay, D. H., & Keenan, F. P. 2014, A&A, 566, A99
Keys, P. H., Mathioudakis, M., Jess, D. B., et al. 2011, ApJL, 740, L40
Keys, P. H., Reid, A., Mathioudakis, M., et al. 2019, MNRAS, 488, L53
Keys, P. H., Reid, A., Mathioudakis, M., et al. 2020, A&A, 633, A60
Keys, P. H., Steiner, O., & Vigeesh, G. 2021, RSPTA, 379, 20200182
Kleint, L., Berkefeld, T., Esteves, M., et al. 2020, A&A, 641, A27
Kuckein, C. 2019, A&A, 630, A139
Kuridze, D., Wöger, F., Uitenbroek, H., et al. 2025, ApJL, 985, L23
Liu, Y., Xiang, Y., Erdélyi, R., et al. 2018, ApJ, 856, 17
Martínez González, M. J., Bellot Rubio, L. R., Solanki, S. K., et al. 2012, ApJL, 758, L40
Monin, A. S., & Iaglom, A. M. 1975, Statistical Fluid Mechanics: Mechanics of Turbulence., Vol. 2 (MIT Press), 882
Nagata, S., Tsuneta, S., Suematsu, Y., et al. 2008, ApJL, 677, L145
Noori, M., Javaherian, M., Safari, H., & Nadjari, H. 2019, AdSpR, 64, 504
Parker, E. N. 1978, ApJ, 221, 368
Peck, C. L., Rast, M. P., Criscuoli, S., & Rempel, M. 2019, ApJ, 870, 89
Rempel, M. 2014, ApJ, 789, 132
Riethmüller, T. L., Solanki, S. K., Berdyugina, S. V., et al. 2014, A&A, 568, A13
Rimmele, T. R., Warner, M., Keil, S. L., et al. 2020, SoPh, 295, 172
Rincon, F., Barrère, P., & Roudier, T. 2025, A&A, 696, A143
Roberts, B., & Webb, A. R. 1978, SoPh, 56, 5
Roudier, T., Švanda, M., Rieutord, M., et al. 2014, A&A, 567, A138
Sánchez Almeida, J., Bonet, J. A., Viticchié, B., & Del Moro, D. 2010, ApJL, 715, L26
Sánchez Almeida, J., Márquez, I., Bonet, J. A., Domínguez Cerdeña, I., & Muller, R. 2004, ApJL, 609, L91
Scharmer, G. B., Bjelksjo, K., Korhonen, T. K., Lindberg, B., & Petterson, B. 2003, SPIE, 4853, 341
Solanki, S. K. 1993, SSRv, 63, 1
Spruit, H. C. 1979, SoPh, 61, 363
Spruit, H. C., & Zweibel, E. G. 1979, SoPh, 62, 15
Stangalini, M., Verth, G., Fedun, V., et al. 2025, A&A, 695, L11
Steiner, O., Hauschildt, P. H., & Bruls, J. 2001, A&A, 372, L13
Utz, D., del Toro Iniesta, J. C., Bellot Rubio, L. R., et al. 2014, ApJ, 796, 79
Utz, D., Hanslmeier, A., Möstl, C., et al. 2009, A&A, 498, 289
Utz, D., Hanslmeier, A., Muller, R., et al. 2010, A&A, 511, A39
Utz, D., Jurčák, J., Hanslmeier, A., et al. 2013, A&A, 554, A65
Wöger, F., Rimmele, T., Ferayorni, A., et al. 2021, SoPh, 296, 145
Wöger, F., von der Lühe, O., & Reardon, K. 2008, A&A, 488, 375
Xu, L., Yang, Y., Yan, Y., et al. 2021, ApJ, 911, 32
Yang, Y., Ji, K., Feng, S., et al. 2015, ApJ, 810, 88
Yang, Y., Li, X., Bai, X., et al. 2019, ApJ, 887, 129